The evolution and dynamics of the Hunga Tonga plume in the stratosphere

Bernard Legras[1], Clair Duchamp[1], Pasquale Sellitto[2,3], Aurélien Podglajen[1], Elisa Carboni[4], Richard Siddans[4], Jens-Uwe Grooß[5], Sergey Khaykin[6], and Felix Ploeger[5]

[1]Laboratoire de Météorologie Dynamique (LMD-IPSL), UMR CNRS 8539, ENS-PSL, École Polytechnique, Sorbonne Université, Institut Pierre Simon Laplace, Paris, France
[2]Univ. Paris Est Créteil and Université de Paris Cité, CNRS, Laboratoire Interuniversitaire des Systèmes Atmosphériques (LISA-IPSL), Institut Pierre-Simon Laplace, Créteil, France
[3]Istituto Nazionale di Geofisica e Vulcanologia (INGV), Osservatorio Etneo (OE), Catania, Italy
[4]UK Research and Innovation, Science and Technology Facilities Council, Rutherford Appleton Laboratory, Chilton, UK
[5]Institute for Energy and Climate Research: Stratosphere (IEK–7), Forschungszentrum Jülich, Jülich, Germany
[6]Laboratoire Atmosphères, Milieux, Observations Spatiales (LATMOS-IPSL), UMR CNRS 8190, Institut Pierre Simon Laplace, Sorbonne Univ./UVSQ, Guyancourt, France

Correspondence: Bernard Legras (bernard.legras@lmd.ipsl.fr)

Abstract. We use a combination of space-borne instruments to study the unprecedented stratospheric plume after the Hunga Tonga eruption of 15 January 2022. The plume was formed of two initial clouds at 30 and 28 km mostly composed of sub-micronic sulphate particles without ashes, washed-out within the first hours. The large amount of water vapour injected led to a fast conversion of SO_2 to sulphates and induced a descent of the plume over the first three weeks by radiative cooling.

5   While SO_2 returned to background levels by the end of January, the sulphate plume persisted until June, mainly confined between 20°N and 35°S due to the zonal symmetry of the summer stratospheric circulation at 24-25 km. As sulphate particles grew through hydration and coagulation, they sediment and separate from the ascending moisture entrained in the Brewer-Dobson circulation. Sulphate aerosol optical depths derived from the IASI infared sounder show that the aerosol plume was not simply diluted and dispersed passively but rather organized in concentrated patches. Winds from the space-borne Doppler

10   lidar ALADIN/AEOLUS suggest that those structures, generated by shear-induced instabilities, are associated with vorticity anomalies. They likely enhance the duration and impacts of the plume.

1   Introduction

The phreato-magmatic eruption of the Hunga Tonga-Hunga Ha'apai (hereafter Hunga Tonga) of 15 January 2022 is exceptional in several respects. Its explosive intensity is close to that of the eruption of Mount Pinatubo in 1991, with a Volcanic Explosivity

15   Index of ~6 (Poli and Shapiro, 2022). The induced atmospheric Lamb wave circled the globe at least 4 times with an amplitude unseen since the 1883 Krakatau eruption (Matoza et al., 2022; Vergoz et al., 2022). Within a few hours, several successive events injected material up to the mesosphere (Podglajen et al., 2022), with the bulk of the plume being detrained between 26 and 34 km (Carr et al., 2022). A further remarkable fact is that the plume carried an unprecedented amount of water vapour into

the stratosphere, increasing instantaneously its overall water vapour content by ∼10% (Millan et al., 2022). Quite surprisingly,
20 the first satellite data gathered after the event reported a stratospheric SO_2 injection of only 0.5 Tg, on par with much smaller
and less explosive eruptions. This led to an early estimate of negligible climatic impact (Witze, 2022). Here, we report on the
evolution of the stratospheric plume during the first months after the eruption and we advocate that its climatic effect is very
significant due to the amount of water vapour and of the sulphate aerosols which have resulted from a fast conversion. We
focus on the circumnavigation of the plume and proceed from the large-scale to the local patterns.

25   2   The mean zonal pattern

Figure A1 shows the zonal mean stratospheric conditions in January-March. In the domain 21-28 km and 25°S-15°N, they are
characterized by an easterly band with a maximal angular speed of 30°/day at 25 km and 5°S. The diabatic heating rate is
positive everywhere except a narrow region near 27 km over the equator. These conditions are stable during the whole period
(Fig. A1d-g). In April-June, the rotation weakens and changes sign while the warming turns to cooling as a combined effects
30 of the Quasi Biennial Oscillation (QBO) and the seasonal cycle.

Figure 1 shows that after an initial fast latitudinal dispersion, the plume stays mostly confined within the band 35°S-20°N
and evolves slowly in the zonal mean. By mid-February, the plume has already spread all around the Earth. However, the
the Ozone Mapping and Profiler Suite Limb Profiler (OMPS-LP) extinction ratio at the core of the cloud increases in time
and reaches an April maximum. Meanwhile, the Cloud-Aerosol Lidar with Orthogonal Polarisation (CALIOP) scattering ratio
35 decreases. This suggests particle growth. The Microwave Limb Sounder (MLS) water vapour initially correlates very well
with the aerosols but they progressively move apart vertically. By early June, aerosols and moisture appear fully separated,
respectively below and above 25 km. The limb instruments suggest larger vertical plume extension than CALIOP due to the
resolution and viewing geometry (Gorkavyi et al., 2021).

The plume vertical motion calculated as described in Appendix A3 is analysed (Fig. 2) for two latitude ranges and the
40 aerosol radius is estimated by interpreting this motion as a fall speed using Eq. (9.42) of Seinfeld and Pandis (2016). Two
separate descent regimes are identified from observations. For the first phase, Figure 2b and d-e show an initial fast descent
until mid-February, which would imply unrealistically large aerosol sizes. The water vapour follows the aerosol downward
motion, against the rising ERA5 motion. Sellitto et al. (2022) (S2022 hereafter) explain this discrepancy by the cooling effect
of water vapour infrared emission which is unaccounted for in ERA5, and ends when the plume gets diluted and approaches
45 vertically its neutral radiative level.

In the second phase, the diluted water vapour is rising in agreement with ERA5 upwelling, while the aerosols continue
their descent, though at a reduced speed. The descent with respect to the ERA5 air is now compatible with a realistic aerosol
size, which is much smaller and growing. Figure 2e suggests that the aerosol size after growing up to 1.5-2 µm in April starts
shrinking in May.

50 The extinction-to-backscatter ratio, obtained by combining OMPS-LP and CALIOP data, is shown in Fig. 2g. This parameter
is also computed using a Mie code (Fig. 2f). The observed trend of the extinction-to-backscatter ratio with aerosol size is

consistent with the theoretical trend direction for sizes between 1 and 2 µm. Considering that the extinction saturates and decays (Fig. 2a) and the decoupling between the aerosols and moisture, we suggest that the initial growth of the particles was by hydration until mid-March, where the extinction culminates and was followed by coagulation growth over April-May and

55 then by a decay due to evaporation as the ambient air gets drier and the plume is diluted. Coagulation and evaporation are obviously not exclusive and their competition depends on the ambient conditions that vary over space and time (Hamill et al., 1977). It is also apparent from Fig. 1 that the moist layer is less confined than the aerosol layer and extends in latitude beyond the limits of the figure. The extinction-to-backscatter ratio is also smaller on the periphery of the plume (Fig. 2e). Therefore, we expect evaporation of the transported sulphate aerosols to occur at such latitudes.

60 The similarity of the extinction-to-backscatter in those two latitude slices implies common microphysical properties. However, the curves of extinction and backscatter taken separately are very different from mid-February to mid-May as can be inferred from Fig. 2a&c.

3 Composition of the plume

We now consider the history of the aerosol composition of the plume. The sequence in Fig. 3a-d shows, in agreement with

65 Carr et al. (2022), that the ash and ice plume (brown and deep blue) is rapidly washed down within the first day following the eruption. What emerges on the west side are two greenish clouds without any hint of ash (that would appear as yellow/reddish). The early CALIOP section (Fig. 3e-f) shows the two aerosol clouds as high-scattering-ratio patches without depolarization, hence made of small spherical particles. A few days later, the LOAC flight from La Réunion brings confirmation by showing sub-micronic, mainly non-absorbing, particles (Kloss et al., 2022).

70 A further source of information is from the Infrared/Microwave Sounder (IMS) retrieval (Appendix A1.2) of SO_2 column and Sulphate Aerosols Optical Depth (SA/OD). Figure 3g-h shows that the conversion to sulphates started immediately after the eruption suggesting the two clouds seen by CALIOP are composed of almost pure sulphate droplets. The fast conversion of SO_2 to sulphate aeerosols is also discussed by S2022 and Zhu et al. (2022), using observations and chemical/transport modelling, respectively.

75 Four days later (Fig. 4b), the two components of the plume are still separated but have elongated under the zonal shear forming a pair of long strips. Comparing Figs. 4a and b, makes apparent that the conversion to sulphates is almost complete in the strip associated to the western and highest cloud (Fig. 3e) while it is incomplete in the strip associated to the eastern cloud. S2022 show that the western cloud is much moister than the eastern one, offering a likely reason for faster conversion, as also discussed by Zhu et al. (2022). A cloud of almost pure SO_2 is located between Australia and Indonesia (Fig. 4a), at

80 lower altitudes than the other two clouds. Comparing the IMS products to RGB-Ash (Fig. 4c) demonstrates that RGB-Ash shows sulphates rather than SO_2 as usually assumed. The sensitivity of geostationary broad-band products, like RGB-Ash, to sulphates is shown by Sellitto and Legras (2016).

The conversion of remaining SO_2 to sulphates proceeds until SO_2 returns to background conditions by late January (Fig. 4d). The sulphates persist for several months and the comparison of Fig. 4e and f shows that zonal averages of IMS and CALIOP products exhibit very similar patterns. The CALIOP depolarization never exceeds its initial value (Fig. 3f) until June.

4   Circumnavigation and instabilities

Figure 5 shows the circumnavigation of the sulphate plumes from a series of IMS SA/OD maps over one month and half. The supplement movie (B) provides an extended view until 30 April. Due to the differential rotation, the fastest patches near 5°S caught the slowest by 30°S by mid-February and the plume filled the whole latitude circle. As time proceeds the components of the plume kept elongating and mixed together towards a zonal uniformity (see movie).

However, Figure 5 shows a number of localized concentrated patches which persist and keep forming in the plume one month after the eruption. Figure 6 investigates the structure of some of them and compares the IMS SA/OD to the observations from active instruments. Figure 6a shows an early case during the blackout period of CALIOP on 24 January. Using the Atmospheric Laser Doppler Instrument (ALADIN) (Appendix A1.5), Figure 6b shows that an anticyclonic anomalous shear spans the highest patch (28 km) which is part of the western strip. The same pattern is observed on 28 January (Fig. 6c) across a patch near 11°E (Fig. 5a) which belongs to the eastern strip. A CALIOP section is available (Fig. 6d) which exhibits a "jelly fish" pattern with a head at 26 km connected by a tail to lower altitude patches along an arc of same angular speed (Fig. A1a). This pattern is found repetitively on CALIOP sections and corresponds to the quasi-circular patches often seen in the SA/OD and RGB-Ash maps.

On 30 January 2022, we are back on the western strip (Fig. 6e) and the CALIOP section (Fig. 6f) shows a hairy pattern above the main patch that we interpret as the tail left by the fast descent. Again this pattern is repetitively observed on CALIOP sections across the western strip until mid-February where the fast descent halts.

A remarkable feature in SA/OD maps are the trains of compact elliptical structure linked together by filaments which are visible all along February and early March in Fig. 5 and the supplement movie. This peculiar shape is reminiscent of shear-induced instabilities as documented, e.g., by Juckes (1995), which lead to the formation of a chain of quasi-circular vortices. The suspicion is reinforced by the pattern of a wrapping up tripolar structure seen near 180°E on 11 February (Fig. 6g) and perfectly captured by CALIOP as a core surrounded by two arms at the same level (Fig. 6h). This comparison also reveals the amount of relevant small-scale details retrieved by the IMS product.

Barotropic shear instability requires a reversal of the meridional gradient of absolute vorticity. The mean flow in ERA5 does not satisfy this criterion. A generalized baroclinic instability requires a reversal of the potential vorticity gradient but the mean flow again hardly satisfies this criterion at the required altitude of 25 km (Fig. A2). The very fact that the instability produces aerosol patches suggests they are related to the generation of vorticity. The detection of an anomalous anticyclonic shear across the concentrated patches of the plume by ALADIN supports this hypothesis. However, sulphates are poor absorbers and neither these vortical structures nor their thermal signature have been detected by our present investigation of the ERA5. Therefore, this observation still requires an explanation that we leave for future studies.

5   Discussion and conclusion

The very intense and unusual Hunga Tonga eruption generated an intense and unusual stratospheric plume with a huge amount of injected water vapour. After a fast initial removal of ice and ashes, the bulk of the remaining plume consisted of two main clouds between 26 and 32 km traveling westward due to the prevailing phase of the QBO. The ensuing zonal transport dispersed
120   the plume all around the Earth within a few weeks.

The fast initial descent of the upper part of the plume induced by the radiative water vapour cooling has concentrated the aerosols within a fairly narrow layer, about 2 km thick. The aerosols later continued subsiding at a slower rate under the effect of gravitational sedimentation, whereas the moist layer entrained by the Brewer-Dobson circulation was simultaneously ascending, so that the two layers progressively decoupled. Although a precise sequencing is difficult without quantitative
125   modelling, it is likely that the sulphate aerosols first grew by hydration, then by coagulation and ended by dwindling under evaporation. Our estimation of fall speed and extinction-to-backscatter ratio trends is consistent with a growth up to 1.5-2.0 μm and then a decrease in mean size.

The data show a fast conversion of SO_2 to sulphates enhanced by water vapour and therefore that the initial sulphur injection might have been strongly underestimated. Consistently, S2022 showed that the Hunga Tonga eruption produced the largest
130   stratospheric aerosol perturbation since the Pinatubo eruption in 1991, and suggested a large potential for climatic impacts. By June, the hemispheric stratospheric aerosol optical depth perturbation of the Hunga Tonga plume is twice as large as the peak perturbation of the 2019 Raikoke eruption, and the tropical impact is at least three times as large as any volcanic perturbation since Pinatubo 1991 (OMPS-LP data, not shown here). As the SO_2 emissions for the Raikoke eruption have been estimated at 1.5 Tg (de Leeuw et al., 2021), we assume this value as the lower limit for the Hunga Tonga eruption, three times larger
135   than early estimates (Witze, 2022). The young aerosols seem mostly made of sub-micronic liquid sulphate particles then growing to 1-2 μm due to hydration/coagulation/evaporation. The dispersion of the plume questions the magnitude and the duration of the impact. An early estimate of the plume radiative forcing by S2022 shows that stratospheric aerosol and water vapour perturbations from the eruption may significantly impact the climate system. Given the large greenhouse potential of stratospheric water vapour (Solomon et al., 2010), it was proposed that the dispersed plume has a net warming effect (S2022),
140   in contrast with the cooling expected from stratospheric aerosols.

Finally, we have shown that the plume repetitively generates compact aerosol circular structures in a process that bears similarities with shear instability.

Appendix A: Data and methods

A1   Observations

145   We use data from the following instruments and products.

A1.1 CALIOP

The Cloud-Aerosol Lidar with Orthogonal Polarisation (CALIOP) is a spaceborne lidar onboard the CALIPSO satellite (Vaughan et al., 2004; Winker et al., 2010). We use the L1 532 nm attenuated backscatter which is filtered in the horizontal with a median filter of width 101 km. In particular, this filter removes the noise associated with the South Atlantic Anomaly

150 (SAA) which perturbs CALIOP data between 30°W and 80°W (Noel et al., 2014). In practice, a limited amount of data are usable in this region and only at night. Due to solar activity, CALIOP was not operating on 18 January and between 20 and 26 January. Hence, our CALIOP series start on 27 January. We use only night data in this work. The molecular backscatter is calculated following Hostetler et al. (2006).

A1.2 IMS

155 The RAL (Rutherford Appleton Laboratory) Infrared/Microwave Sounder (IMS) retrieval core scheme (Siddans, 2019) uses an optimal estimation spectral fitting procedure to retrieve atmospheric and surface parameters jointly from co-located measurements by IASI (Infrared Atmospheric Sounding Interferometer), AMSU (Advanced Microwave Sounding Unit) and MHS (Microwave Humidity Sounder) on MetOp-B spacecraft, using RTTOV 12 (Radiative Transfer for TOVS)(Saunders et al., 2017) as the forward radiative transfer model. The use of RTTOV 12 enables the quantitative retrieval of volcanic-specific

160 aerosols (sulphate aerosol) and trace gases (SO_2). The present paper uses IMS SO_2 and sulphate aerosols observations from its near-real time implementation. The IMS scheme retrieves the SO_2 in the sensitive region around 1100-1200 cm^{-1}, in ppbv assuming a uniform vertical mixing ratio. It retrieves sulphate-specific AOD (Aerosol Optical Depth) at 1200 cm^{-1} (i.e. the peak of the mid-infrared extinction cross section (Sellitto and Legras, 2016)), assuming a Gaussian extinction coefficient profile shape peaking at 20 km altitude, with 2 km full-width half-maximum. The bulk of the spectroscopic information on SO_2

165 and sulphate aerosols, in the IMS scheme, thus comes from the IASI Fourier transform spectrometer (Clerbaux et al., 2009). We refer to the two retrieved product as IMS $SO-2$ and IMS SA/OD in this work.

A1.3 OMPS-LP

The Ozone Mapping and Profiler Suite Limb Profiler (OMPS-LP) onboard the Suomi-NPP satellite provides along track vertical profiles of aerosol extinction in several visible bands (Loughman et al., 2018; Taha and Loughman, 2020). We use version

170 2.1 and the 745 nm band as recommended by Taha et al. (2021). Swaths with non zero quality flag are discarded. Basically, this filters data polluted by the SAA but filtered and non filtered results differ very little in our processing. The molecular extinction is calculated from the same formulas as the CALIOP molecular backscatter but for a change of wavelength.

A1.4 MLS

The Microwave Limb Sounder (MLS) onboard NASA's AURA satellite provides along track vertical profiles of water vapour

175 mixing ratio (Lambert et al., 2015). We use the version 4 without accounting the quality flag as in Millan et al. (2022).

A1.5 ALADIN

The Atmospheric Laser Doppler Instrument (ALADIN) onboard the Aeolus satellite is the first space-borne Doppler wind lidar. It is designed to measure wind along the line of sight from the Doppler shift of the 355 nm light emitted by the laser and scattered back by molecules (Rayleigh wind) or aerosols (Mie wind). Horizontal line-of-sight wind is retrieved neglecting the vertical wind component. The anomaly wind is calculated by removing the background wind at same time and location from ERA5. As the line-of-sight is perpendicular to the heliosynchronous orbit, the measured component at low and mid-latitudes is essentially the zonal wind. The ceiling of Aeolus vertical bins can be adjusted and was increased to 30 km in the area of the Hunga Tonga plume (30°S-0°) a few days after the eruption. At high altitude, the Mie product is of better quality inside the plume and is used in the present study.

A1.6 RGB-Ash

We use a composite RGB product, denoted as RGB-Ash, that benefits from the sensitivity of the 8.5 μm band of the Advanced Himawari Imager (AHI) and Spanning Enhanced Visible and InfraRed Imager (SEVIRI) onboard the geostationary Himawari-8 and Meteosat-8 satellites. The product is based on the EUMETSAT Ash RGB recipe (https://navigator.eumetsat.int/product/EO:EUM:DAT:MSG:VOLCANO/print) and uses the brightness temperatures (BT in K) of the three channels: 8.5, 10.4 and 12.3 μm. The recipe for the three colour indexes ranging from 0 to 1 is $R = (\mathrm{BT}(12.3) - \mathrm{BT}(10.4) + 2574)/6$, $G = (\mathrm{BT}(10.4) - \mathrm{BT}(8.5) + 4)/9$ and $B = (\mathrm{BT}(10.4) - 243)/60$. The same recipe is used for both instruments even if the channels are not strictly identical. This product allows to qualitatively distinguish thick ash plumes or ice clouds (brown), thin ice clouds (dark blue) and sulphur-containing plumes (green). Mixed ash/sulphur-containing volcanic species would appear in reddish and yellow shades.

A2 ERA5 reanalysis and meteorological data

We use the European Center for Medium Range Forecasts ERA5 reanalysis (Hersbach et al., 2020) at $1° \times 1°$ resolution and the model levels with 6-hourly sampling. The data are averaged daily and zonally. The total all sky radiative heating rate is converted into diabatic vertical velocity from the relation between geopotential and potential temperature. The motion of the potential temperature lines with respect to the geopotential in the zonal mean is used to define the adiabatic vertical velocity. The ERA5 does not assimilate the anomalous water vapour or the aerosols in the stratosphere and therefore cannot account for their direct radiative effect. It can only assimilate the induced local temperature perturbation if large enough and then react to damp it (Lestrelin et al., 2021). In the present case, the temperature assimilation is further perturbed by the effect of water vapour on the GPS or the infrared signals.

The Lait potential vorticity (LPV) used in Fig.A2 is defined from the Ertel potential vorticity (PV) as

$$\mathrm{LPV} = \left(\frac{600}{\theta}\right)^4 \mathrm{PV},$$

where θ is the potential temperature in K.

A3   Vertical motion from CALIOP and MLS

The observed vertical motion is obtained from CALIOP and MLS by applying a second-order Savitsky-Golay filter with a 21-day window to the daily mean vertical location of CALIOP scattering ratio and MLS water vapour, retaining data above 2 and 6 ppmv offsets, respectively. In order to compensate for background air motion and the motion of isentropic surfaces with respect to geopotential surfaces, the diabatic and adiabatic background vertical velocity are calculated from ERA5. The diabatic motion results from the total radiative heating rate $\frac{DT}{Dt}|_{\mathrm{RAD}}$ multiplied by $\frac{\theta}{T}\frac{\delta z}{\delta \theta}$ where (T, θ, z) are temperature, potential temperature and geopotential altitude. The adiabatic motion, which is always a small correction, is estimated as $-\frac{\partial \theta}{\partial t}|_p \frac{\delta z}{\delta \theta} + \frac{\partial z}{\partial t}|_p$. The calculations are made by centered finite differences on the model grid which is in pure pressure in the considered latitude range. A resulting corrected aerosol motion with respect to the ERA5 air is then calculated by removing the diabatic and adiabatic motions from the observed vertical motion.

A4   Mie calculations

The theoretical extinction-to-backscatter ratio for the plume has been calculated using the Python-based miepython Mie code, available at: https://miepython.readthedocs.io/en/latest/. The extinction and backscatter coefficients have been estimated at 750 and 532 nm, respectively, to simulate OMPS and CALIOP observations. Typical sulphate aerosols refractive indices have been considered, with the assumption of very weakly absorbing particles (based on the results of (Kloss et al., 2022)). Log-normal size distributions with varying standard deviation are simulated, to study how this ratio changes with radius.

Appendix B: IMS animation

The animation https://mycore.core-cloud.net/index.php/s/CQdtD1VLY2xYuKe shows the IMS SA/OD product for all day and night orbits of each day between 13 January and 30 April 2022. The indicated times are those of the intersection of the orbits with the equator. When two orbit swaths overlap, the crossing time of the overlapped orbit is indicated in red. Missing orbits are blanked out. Several days are entirely missing between 8 and 14 March.

Code and data availability.   MLS and OMPS-LP data are available from EarthData centre at: https://disc.gsfc.nasa.gov/. CALIOP data v3.41 are available at: https://doi.org/10.5067/CALIOP/CALIPSO/CAL_LID_L1-VALSTAGE1-V3-41. ALADIN data are available from ESA at https://earth.esa.int/eogateway/missions/aeolus/data. IMS data will be available on a public deposit. ERA5 data are available at https://www.ecmwf.int/en/forecasts/datasets/reanalysis-datasets/era5. The python scripts and notebooks used in this study will be available at https://github.com/bernard-legras/ASTuS and the intermediate datasets will be available from Zenodo. In the mean time, send requirements to the corresponding author

Video supplement.   https://mycore.core-cloud.net/index.php/s/CQdtD1VLY2xYuKe

235 *Author contributions.* BL, PS and AP conceived the study and conducted the analyses. EC and RS elaborated and provided the IMS product. JUG, SK and FP were involved in discussions of the results and their interpretation. The paper was written by BL, CD, PS and AP. All authors contributed to the final version.

Competing interests. The authors declare no competing interests.

Acknowledgements. The CALIOP and GEOs data have been provided by the AERIS/ICARE Data and Service Centre and processed using
240 the centre computer resoources. ERA5 data were provided by Copernicus Climate Change Service. We acknowledge support from the Agence Nationale de la Recherche under grants 21-CE01-0007-01 (ASTuS), 21-CE01-0028-01 (TuRTLES) and 21-CE01-0028-01 (PyroStrat). We acknowledge discussions with Paul Billant, Guillaume Carazzo, Corinna Kloss, Guillaume Lapeyre, Angela Limare and Tjarda Roberts.

References

Carr, J. L., Horvath, A., Wu, D. L., and Friberg, M. D.: Stereo Plume Height and Motion Retrievals for the Record-Setting Hunga Tonga-
245   Hunga Ha'apai Eruption of 15 January 2022, Geophysical Research Letters, https://doi.org/10.1029/2022GL098131, 2022.

Clerbaux, C., Boynard, A., Clarisse, L., George, M., Hadji-Lazaro, J., Herbin, H., Hurtmans, D., Pommier, M., Razavi, A., Turquety, S.,
       Wespes, C., and Coheur, P.-F.: Monitoring of atmospheric composition using the thermal infrared IASI/MetOp sounder, Atmospheric
       Chemistry and Physics, 9, 6041–6054, https://doi.org/10.5194/acp-9-6041-2009, 2009.

de Leeuw, J., Schmidt, A., Witham, C. S., Theys, N., Taylor, I. A., Grainger, R. G., Pope, R. J., Haywood, J., Osborne, M., and Kristiansen,
250   N. I.: The 2019 Raikoke volcanic eruption – Part 1: Dispersion model simulations and satellite retrievals of volcanic sulfur dioxide,
       Atmospheric Chemistry and Physics, 21, 10 851–10 879, https://doi.org/10.5194/acp-21-10851-2021, 2021.

Gorkavyi, N., Krotkov, N., Li, C., Lait, L., Colarco, P., Carn, S., DeLand, M., Newman, P., Schoeberl, M., Taha, G., Torres, O., Vasilkov, A.,
       and Joiner, J.: Tracking aerosols and SO₂ clouds from the Raikoke eruption: 3D view from satellite observations,
       Atmospheric Measurement Techniques, 14, 7545–7563, https://doi.org/10.5194/amt-14-7545-2021, 2021.

255 Hamill, P., Toon, O. B., and Kiang, C. S.: Microphysical Processes Affecting Stratospheric Aerosol Particles, Journal of the Atmospheric
       Sciences, 34, 1104–1119, https://doi.org/10.1175/1520-0469(1977)034<1104:MPASAP>2.0.CO;2, 1977.

Hersbach, H., Bell, B., Berrisford, P., Hirahara, S., Horányi, A., Muñoz-Sabater, J., Nicolas, J., Peubey, C., Radu, R., Schepers, D., Simmons,
       A., Soci, C., Abdalla, S., Abellan, X., Balsamo, G., Bechtold, P., Biavati, G., Bidlot, J., Bonavita, M., Chiara, G., Dahlgren, P., Dee,
       D., Diamantakis, M., Dragani, R., Flemming, J., Forbes, R., Fuentes, M., Geer, A., Haimberger, L., Healy, S., Hogan, R. J., Hólm, E.,
260   Janisková, M., Keeley, S., Laloyaux, P., Lopez, P., Lupu, C., Radnoti, G., Rosnay, P., Rozum, I., Vamborg, F., Villaume, S., and Thépaut,
       J.: The ERA5 global reanalysis, Quarterly Journal of the Royal Meteorological Society, 146, 1999–2049, https://doi.org/10.1002/qj.3803,
       2020.

Hostetler, C. A., Liu, Z., Reagan, J. A., Vaughan, M., Winker, D., Osborn, M., Hunt, W. H., Powell, K. A., and Trepte, C.: CALIOP Algorithm
       Theoretical Basis Document. Calibration and Level 1 Data Products, Tech. Rep. Doc. PS-SCI-201, NASA Langley Res. Cent., Hampton,
265   VA, https://www-calipso.larc.nasa.gov/resources/pdfs/PC-SCI-201v1.0.pdf, 2006.

Juckes, M.: Instability of surface and upper-tropospheric shear lines, J. Atmos. Sci., 52, 3247–3262, 1995.

Kloss, C., Sellitto, P., renard, j.-b., Baron, A., Begue, N., Legras, B., Berthet, G., Briaud, E., Carboni, E., Duchamp, C., Duflot, V., Jacquet,
       P., Marquestaut, N., Metzger, J.-M., Payen, G., Ranaivombola, M., Roberts, T., Siddans, R., and Jegou, F.: Aerosol characterization of the
       stratospheric plume from the volcanic eruption at Hunga Tonga January 15th 2022, https://doi.org/10.1002/essoar.10511312.1, 2022.

270 Lambert, A., Livesey, N. J., and Read, W.: MLS/Aura L2 Water Vapor (H2O) Mixing Ratio - Version 4,
       https://doi.org/10.5067/AURA/MLS/DATA2009, type: dataset, 2015.

Lestrelin, H., Legras, B., Podglajen, A., and Salihoglu, M.: Smoke-charged vortices in the stratosphere generated by wildfires and their
       behaviour in both hemispheres: comparing Australia 2020 to Canada 2017, Atmospheric Chemistry and Physics, 21, 7113–7134,
       https://doi.org/10.5194/acp-21-7113-2021, 2021.

275 Loughman, R., Bhartia, P. K., Chen, Z., Xu, P., Nyaku, E., and Taha, G.: The Ozone Mapping and Profiler Suite (OMPS) Limb Pro-
       filer (LP) Version 1 aerosol extinction retrieval algorithm: theoretical basis, Atmospheric Measurement Techniques, 11, 2633–2651,
       https://doi.org/10.5194/amt-11-2633-2018, 2018.

Matoza, R. S., Fee, D., Assink, J. D., Iezzi, A. M., Green, D. N., Kim, K., Toney, L., Lecocq, T., Krishnamoorthy, S., Lalande, J.-M., Nishida,
       K., Gee, K. L., Haney, M. M., Ortiz, H. D., Brissaud, Q., Martire, L., Rolland, L., Vergados, P., Nippress, A., Park, J., Shani-Kadmiel, S.,

280   Witsil, A., Arrowsmith, S., Caudron, C., Watada, S., Perttu, A. B., Taisne, B., Mialle, P., Le Pichon, A., Vergoz, J., Hupe, P., Blom, P. S., Waxler, R., De Angelis, S., Snively, J. B., Ringler, A. T., Anthony, R. E., Jolly, A. D., Kilgour, G., Averbuch, G., Ripepe, M., Ichihara, M., Arciniega-Ceballos, A., Astafyeva, E., Ceranna, L., Cevuard, S., Che, I.-Y., De Negri, R., Ebeling, C. W., Evers, L. G., Franco-Marin, L. E., Gabrielson, T. B., Hafner, K., Harrison, R. G., Komjathy, A., Lacanna, G., Lyons, J., Macpherson, K. A., Marchetti, E., McKee, K. F., Mellors, R. J., Mendo-Pérez, G., Mikesell, T. D., Munaibari, E., Oyola-Merced, M., Park, I., Pilger, C., Ramos, C., Ruiz, M. C., Sabatini,

285   R., Schwaiger, H. F., Tailpied, D., Talmadge, C., Vidot, J., Webster, J., and Wilson, D. C.: Atmospheric waves and global seismoacoustic observations of the January 2022 Hunga eruption, Tonga, Science, https://doi.org/10.1126/science.abo7063, 2022.

Millan, L., Santee, M. L., Lambert, A., Livesey, N. J., Werner, F., Schwartz, M. J., Pumphrey, H. C., Manney, G. L., Wang, Y., Su, H., Wu, L., Read, W. G., and Froidevaux, L.: Hunga Tonga-Hunga Ha'apai Hydration of the Stratosphere, preprint, in review, https://doi.org/10.1002/essoar.10511266.1, 2022.

290   Noel, V., Chepfer, H., Hoareau, C., Reverdy, M., and Cesana, G.: Effects of solar activity on noise in CALIOP profiles above the South Atlantic Anomaly, Atmospheric Measurement Techniques, 7, 1597–1603, https://doi.org/10.5194/amt-7-1597-2014, 2014.

Podglajen, A., Le Pichon, A., Garcia, R. F., Gerier, S., Millet, C., Bedka, K. M., Khlopenkov, K. V., Khaykin, S. M., and Hertzog, A.: Balloon-borne observations of acoustic-gravity waves from the 2022 Hunga Tonga eruption in the stratosphere, Earth and Space Science Open Archive, p. 16, https://doi.org/10.1002/essoar.10511570.1, 2022.

295   Poli, P. and Shapiro, N. M.: Rapid Characterization of Large Volcanic Eruptions: Measuring the Impulse of the Hunga Tonga Ha'apai Explosion From Teleseismic Waves, Geophysical Research Letters, 49, https://doi.org/10.1029/2022GL098123, 2022.

Saunders, R., Hocking, J., Rundle, D., Rayer, P., Hayemann, S., Matricardi, A., Lupu, C., Brunel, P., and Vidot, J.: RTTOV-12 SCIENCE AND VALIDATION REPORT; Version : 1.0, Doc ID : NWPSAF-MO-TV-41, https://nwp-saf.eumetsat.int/site/download/documentation/rtm/docs_rttov12/rttov12_svr.pdf, 2017.

300   Seinfeld, J. H. and Pandis, S. N.: Atmospheric chemistry and physics: from air pollution to climate change, John Wiley & Sons, ISBN:978-1-119-22116-6 978-1-119-22117-3 Third edition,, 2016.

Sellitto, P. and Legras, B.: Sensitivity of thermal infrared nadir instruments to the chemical and microphysical properties of UTLS secondary sulfate aerosols, Atmospheric Measurement Techniques, 9, 115–132, https://doi.org/10.5194/amt-9-115-2016, 2016.

Sellitto, P., Podglajen, A., Belhadji, R., Boichu, M., Carboni, E., Cuesta, J., Duchamp, C., Kloss, C., Siddans, R., Begue, N., Blarel, L.,

305   Jegou, F., Khaykin, S., Renard, J.-B., and Legras, B.: The unexpected radiative impact of the Hunga Tonga eruption of January 15th, 2022, preprint, in review, https://doi.org/10.21203/rs.3.rs-1562573/v1, 2022.

Siddans, R.: Water Vapour Climate Change Initiative (WV-CCI) - Phase One, Deliverable 2.2; Version 1.0, https://climate.esa.int/documents/1337/Water_Vapour_CCI_D2.2_ATBD_Part2-IMS_L2_product_v1.0.pdf, 2019.

Solomon, S., Rosenlof, K. H., Portmann, R. W., Daniel, J. S., Davis, S. M., Sanford, T. J., and Plattner, G.-K.: Contributions of stratospheric

310   water vapor to decadal changes in the rate of global warming., Science, 327, 1219–1223, https://doi.org/10.1126/science.1182488, 2010.

Taha, G. and Loughman, R.: OMPS-NPP L2 LP Aerosol Extinction Vertical Profile swath daily 3slit V2, https://doi.org/10.5067/CX2B9NW6FI27, type: dataset, 2020.

Taha, G., Loughman, R., Zhu, T., Thomason, L., Kar, J., Rieger, L., and Bourassa, A.: OMPS LP Version 2.0 multi-wavelength aerosol extinction coefficient retrieval algorithm, Atmospheric Measurement Techniques, 14, 1015–1036, https://doi.org/10.5194/amt-14-1015-

315   2021, 2021.

Vaughan, M. A., Young, S. A., Winker, D. M., Powell, K. A., Omar, A. H., Liu, Z., Hu, Y., and Hostetler, C. A.: Fully automated analysis of space-based lidar data: an overview of the CALIPSO retrieval algorithms and data products, Proc. SPIE 5575, Laser Radar Techniques for Atmospheric Sensing, (4 November 2004), https://doi.org/10.1117/12.572024, 2004.

Vergoz, J., Hupe, P., Listowski, C., Le Pichon, A., Garcés, M., Marchetti, E., Labazuy, P., Ceranna, L., Pilger, C., Gaebler, P., Näsholm, S., Brissaud, Q., Poli, P., Shapiro, N., De Negri, R., and Mialle, P.: IMS observations of infrasound and acoustic-gravity waves produced by the January 2022 volcanic eruption of Hunga, Tonga: A global analysis, Earth and Planetary Science Letters, 591, 117 639, https://doi.org/10.1016/j.epsl.2022.117639, 2022.

Winker, D. M., Pelon, J., Coakley, J. A., Ackerman, S. A., Charlson, R. J., Colarco, P. R., Flamant, P., Fu, Q., Hoff, R. M., Kittaka, C., Kubar, T. L., Le Treut, H., Mccormick, M. P., Mégie, G., Poole, L., Powell, K., Trepte, C., Vaughan, M. A., and Wielicki, B. A.: The CALIPSO Mission: A Global 3D View of Aerosols and Clouds, Bulletin of the American Meteorological Society, 91, 1211–1230, https://doi.org/10.1175/2010BAMS3009.1, 2010.

Witze, A.: Why the Tongan eruption will go down in the history of volcanology, Nature, 602, 376–378, https://doi.org/10.1038/d41586-022-00394-y, 2022.

Zhu, Y., Bardeen, C., Tilmes, S., Mills, M., Harvey, V., Taha, G., Kinnison, D., Yu, P., Rosenlof, K., Wang, X., Avery, M., Kloss, C., Li, C., Glanville, A., Millan, L., Deshler, T., Portmann, R., Krotkov, N., and Toon, O.: 2022 Hunga-Tonga eruption: stratospheric aerosol evolution in a water-rich plume, preprint, in review, https://doi.org/10.21203/rs.3.rs-1647643/v1, 2022.
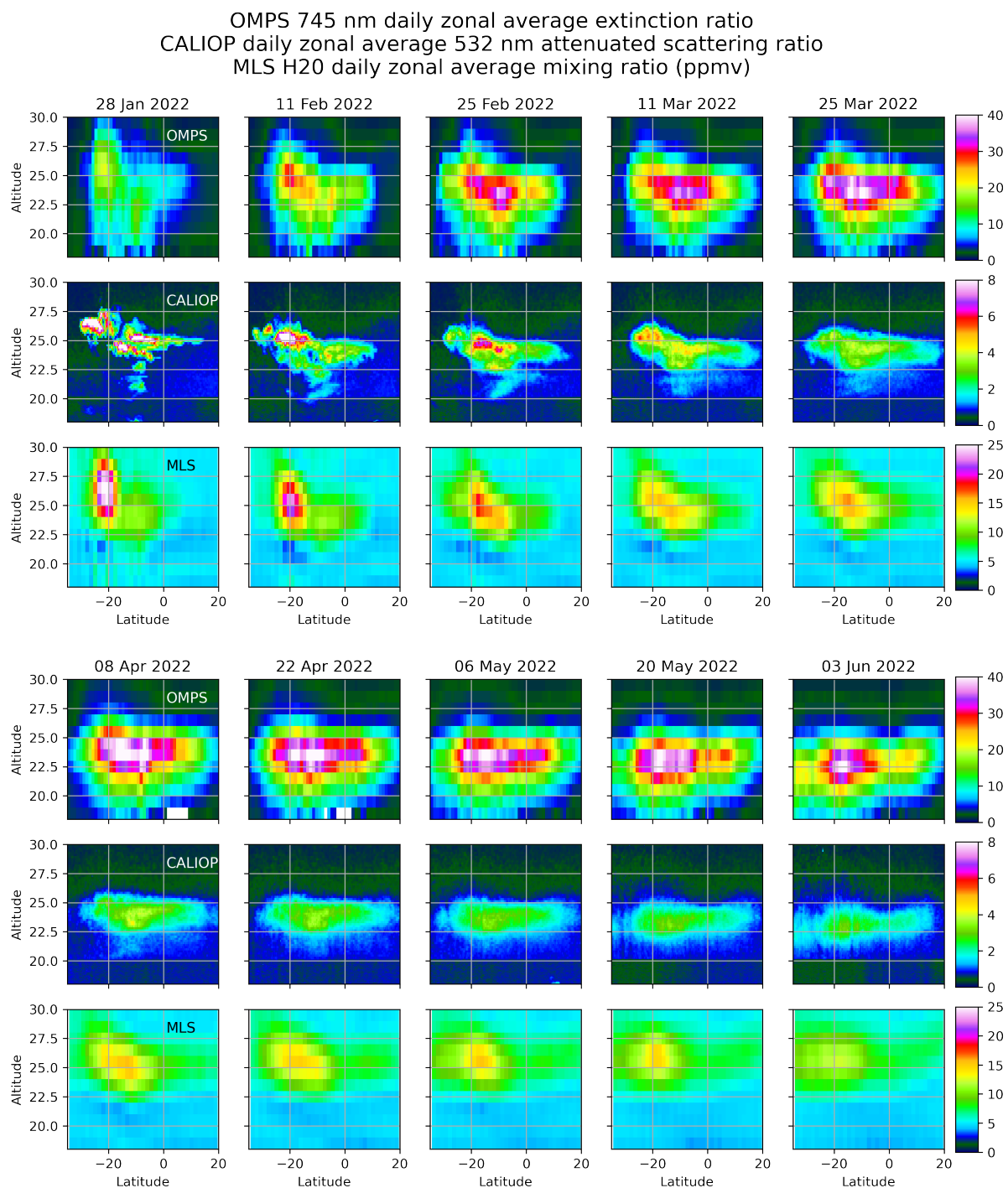
Figure 1. Series of daily zonal averages over all available orbits from three satellites measuring aerosols and water vapour (Appendices A1.3, A1.1 and A1.4). The series is shown in two consecutive blocks of three rows. Upper row: OMPS-LP 745 nm aerosol extinction ratio. Middle row: CALIOP 532 nm aerosol attenuated backscatter ratio. Lower row: MLS water vapour (in ppmv). Days from 28/01/2022 to 04/06/2022 with 16-day step.
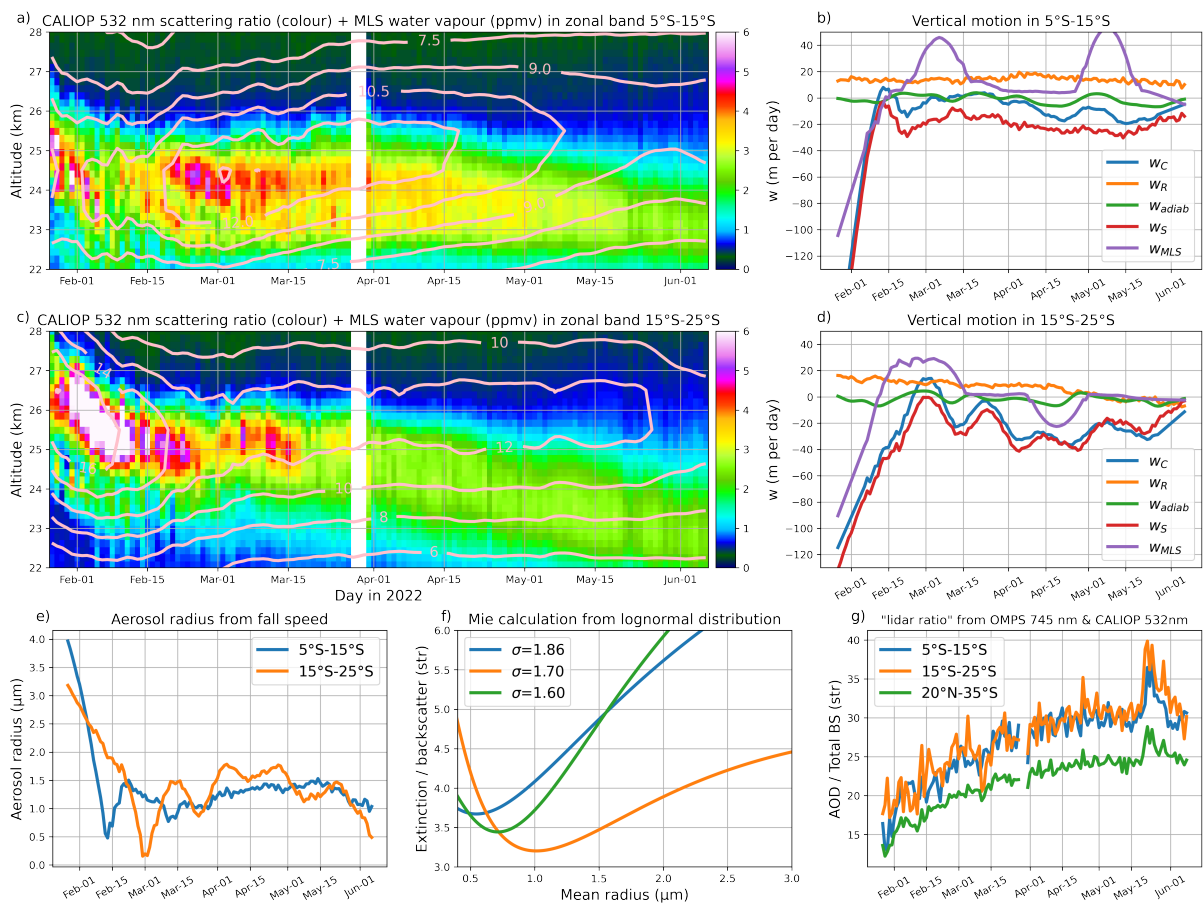
Figure 2. (a) and (c) Zonal and latitude band averages as a function of time for CALIOP 532 nm scattering ratio (colour) and MLS water vapour (contours, ppmv) for, respectively 5°-15°S and 15°-25°S latitude bands. (b) and (d) Vertical motions for the same two latitude bands: W_C for aerosol and w_{MLS} for water vapour deduced from (a) and (c), w_R and w_{adiab} for ERA5 diabatic and adiabatic vertical motion, and for the resulting vertical motion of the aerosols with respect to the ERA5 air (e) Aerosol radius deduced from w_S interpreted as aerosol fall speed and using Eq. (9.42) of Seinfeld and Pandis (2016). (f) Ratio of the theoretical 745 nm aerosol extinction and 532 nm aerosol backscatter cross sections, calculated using a Mie code (see Appendix A4) with three values of the standard deviation σ. (g) Ratio of the 745 nm OMPS LP aerosol optical depth and 532 nm CALIOP integrated attenuated backscatter, both over the range 18 to 30 km.
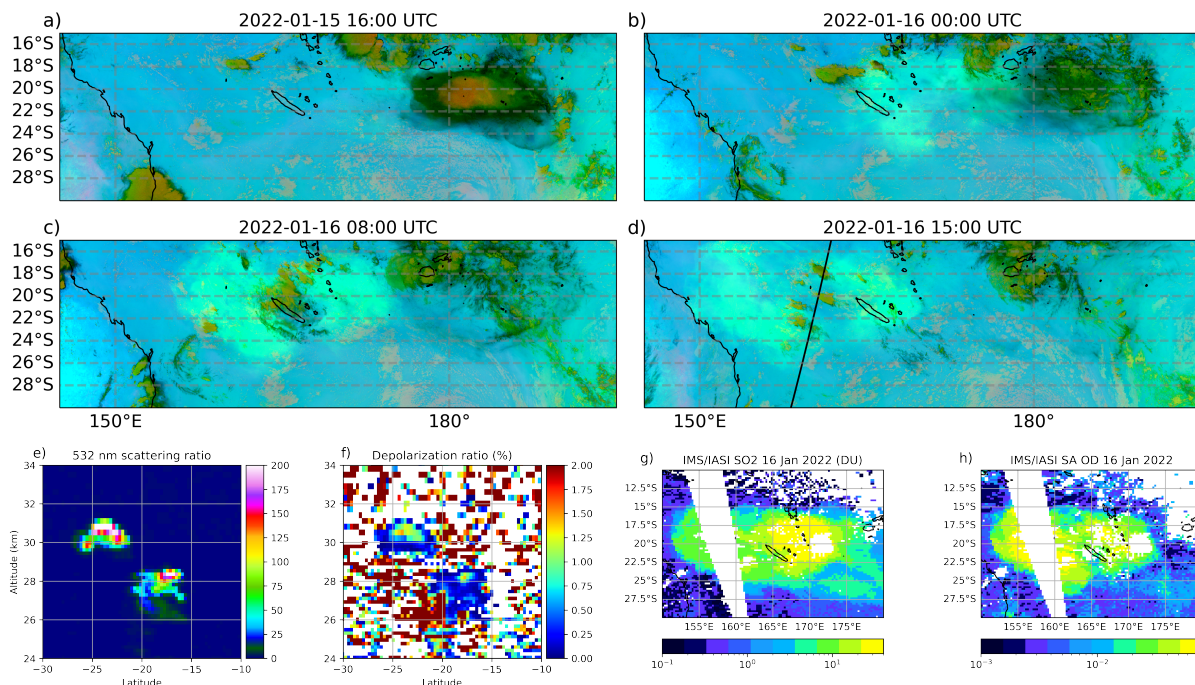
Figure 3. (a-d) RGB-Ash composite (see Appendix A1.6) from Himawari-8 at four selected times during the first day and half following the eruption. (e) CALIOP 532 nm backscatter ratio along the orbit track shown in (d) at 15:08 UTC. (f) 532 nm depolarization ratio (orthogonal channel / total) for the same orbit. (g-h) SA/OD and SO_2 from IMS on 16/02/20222 for two night orbits crossing the equator at 10:26 UTC (right swath) and 12:08 UTC (left swath).
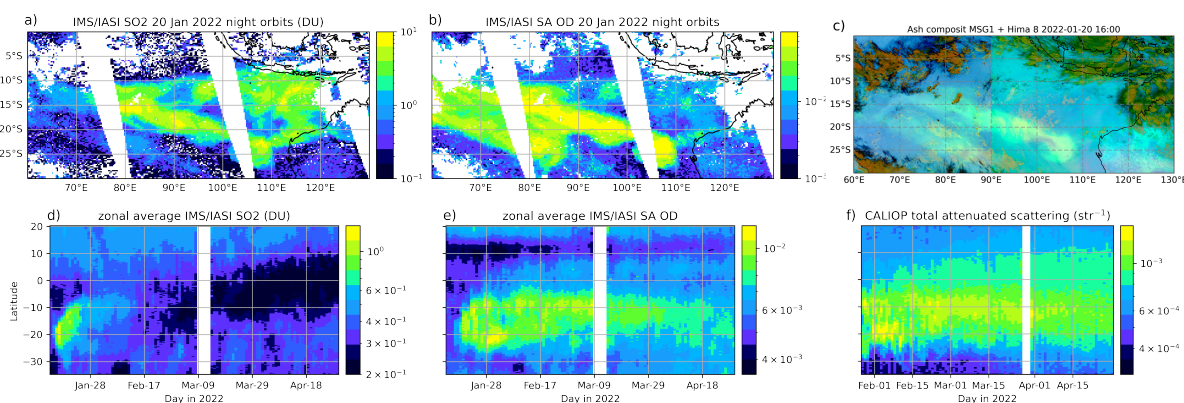
Figure 4. (a-b) SA/OD and SO_2 from IMS on 20/01/2022 for three night orbits crossing equator at 14:06 UTC (right swath), 15:48 UTC (middle swath) and 17:29 UTC. (c) RGB-Ash composite from Meteosat-8 and Himawari-8 at 16:00 UTC on the same day. (d-e) Zonal average SA OD and SO_2 from 13/01/2022 to 30/04/2022 (f) CALIOP 532 nm attenuated backscatter integrated between 18 and 30 km from 27/01/2022 to 30/04/2022 (in str^{-1}).
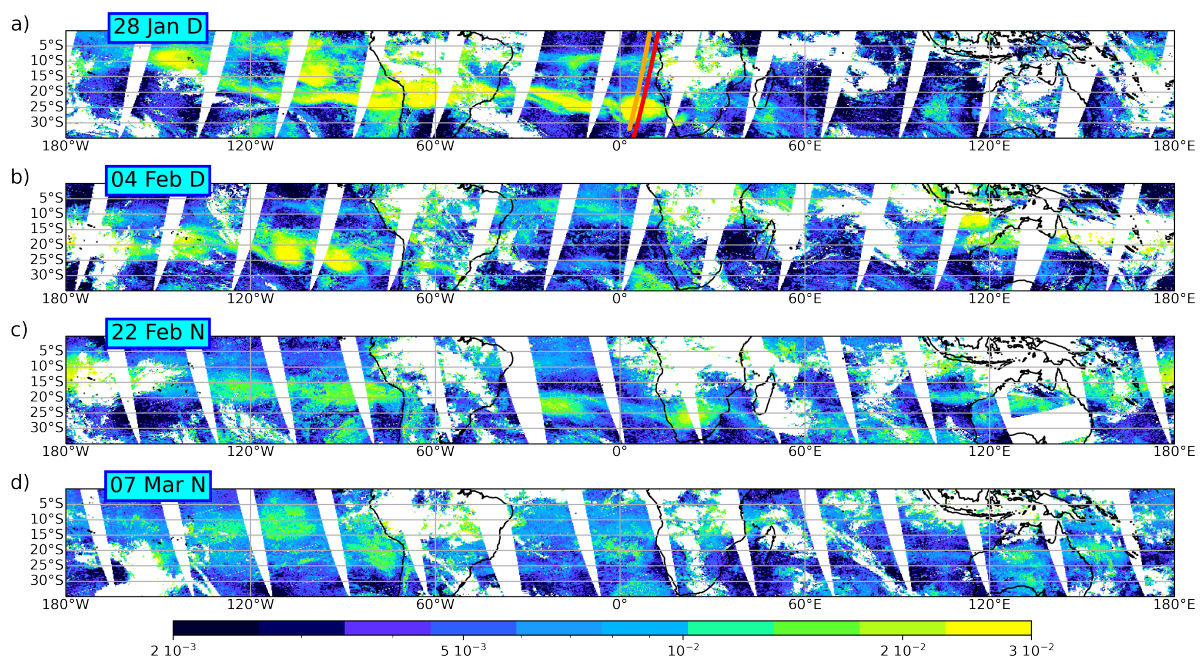
Figure 5. SA/OD from IMS in the latitude range 0°-35°S at four different dates as indicated. Panels a and b are drawn for night swaths while panels c and d are drawn for day swaths.
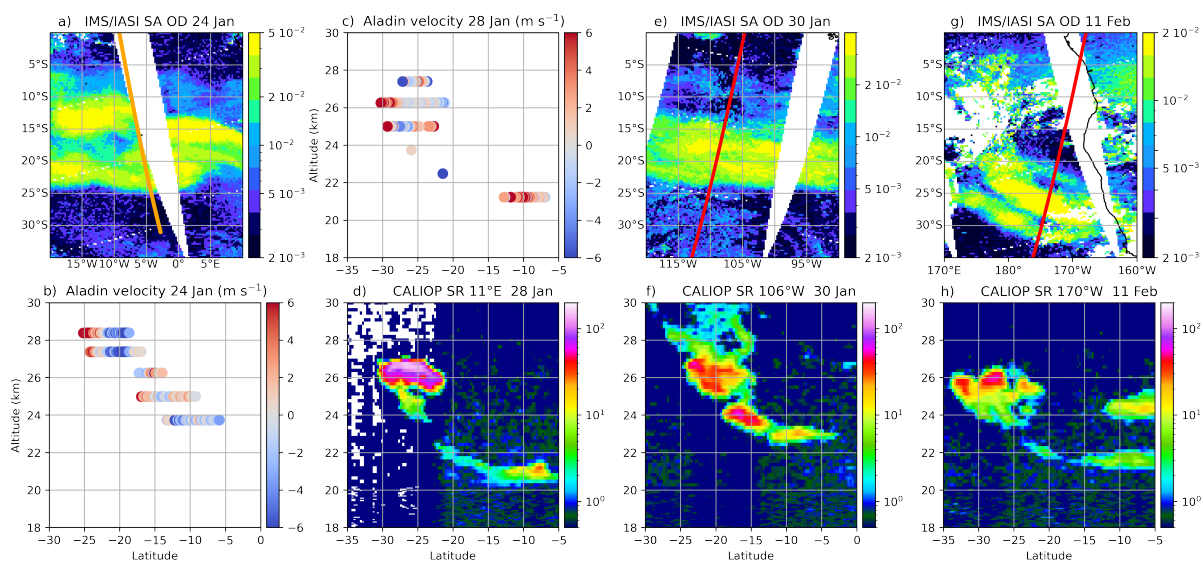
Figure 6. a) IMS SA/OD chart on 24 January 2022 near 22:52 UTC for the left swath. b) ALADIN wind anomaly on 24 January 2022 near 18:36 UTC along the track shown in panel a). c) ALADIN wind anomaly near 5:12 UTC on 28 January 2022 along the the orange track shown on Fig. 5a within the IASI 8:48 UTC swath on the same day. d) CALIOP 522 nm scattering ratio on 28 January 2022 near 1:48 UTC along the red track on Fig. 5a. e) IMS SA/OD chart on 30 January 2022 near 11:28 UTC for the left swath. f) CALIOP 522 nm scattering ratio on 30 January 2022 near 9:37 UTC along the red track on panel e). g) Same as e) for 11 February near 9:49 UTC. h) Same at f) for 11 February near 13:52 UTC and the red track on panel g).
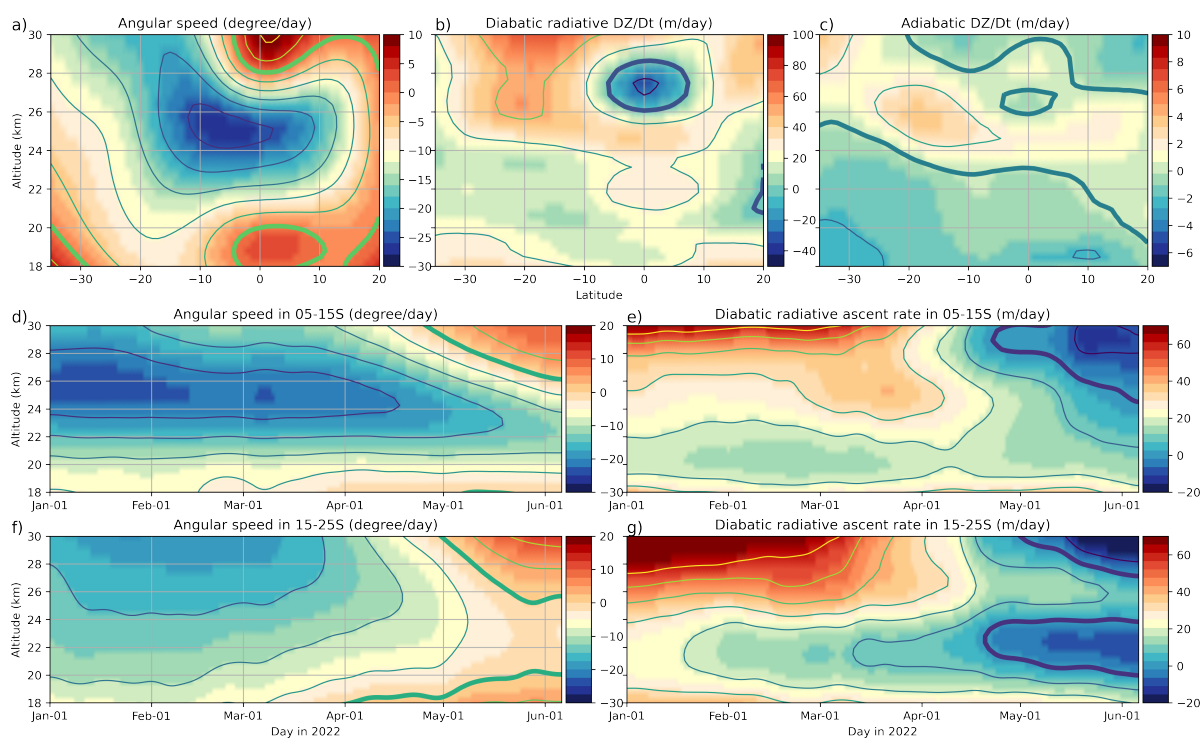
Figure A1. (a) Zonal mean angular rotation speed $\omega = \frac{U}{R_{\mathrm{Earth}}\cos(\phi)}$ from ERA5 averaged between 15/01/2022 and 15/03/2022 (in degree day^{-1}). (b) Same for the diabatic ascent calculated from the total all-sky ERA5 heating rate (in m day^{-1}). (c) Same for the adiabatic ascent due to motion of the isentropic surfaces with respect to the geopotential surfaces (in m day^{-1}). (d) Daily zonal and altitude band average angular speed between 5°S and 15°S as a function of time (in degree day^{-1}). (e) Same as d) for the diabatic ascent (in m day^{-1}). (f-g) same as (d-e) for the latitude band between 15°S and 25°S.
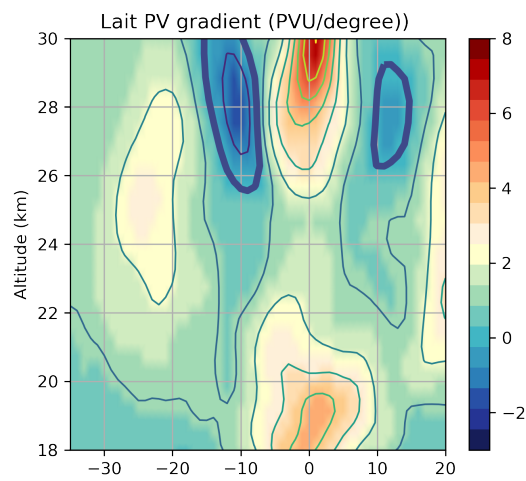
Figure A2. Meridional gradient of the zonal and time average Lait PV defined in Appendix A2. The unit is PVU per degree where 1 PVU = $10^6 \mathrm{m^2 s^{-1} K kg^{-1}}$.